Islamic Azad University

Journal of
Optoelectronical Nanostructures

Summer 2024 / Vol. 9, No. 3

## Research Paper

# Analysis and Simulation of the Schottky Junction Using an Ensemble Monte Carlo Model

**Fatemeh Haddadan[1], Mohammad Soroosh*[,1], Ramakrishnan Rajasekar [2]**

[1] Department of Electrical Engineering, Shahid Chamran University of Ahvaz, Ahvaz, Iran.
[2] Department of Electronics and Communication Engineering, SRM Institute of Science and Technology, Tiruchirappalli, India

**Received:** 15 Feb. 2024
**Revised:** 14 Mar. 2024
**Accepted:** 5 Jun. 2024
**Published:** 15 Sep. 2024

**Keywords:**
**Electron Scattering, Monte Carlo Model, Schottky Junction, Thermionic Emission, Tunneling.**

## Abstract

In this article, an ensemble Monte Carlo model is presented for the Al/n-GaAs Schottky junction using a two-valley regime. The non-parabolic energy bands and electron valleys are considered as Γ and L. Electron scattering mechanisms arising from impurities, optical phonons, and acoustic phonons are assumed, and mechanisms like thermionic emission and tunneling are considered for electron transit through the Schottky barrier. To evaluate the accuracy of the proposed model, the obtained results are compared with data from others. Furthermore, in addition to the potential and electric field distribution in the Schottky junction, the spatial distribution of electrons, energy distribution, velocity distribution, and contributions of various scattering mechanisms are also provided. This microscopic image is one of the prominent features of the proposed model that other numerical models like drift-diffusion and hydrodynamics are not capable of providing.

Citation: Fatemeh Haddadan, Mohammad Soroosh, Ramakrishnan Rajasekar. Analysis and Simulation of The Schottky Junction Using an Ensemble Monte Carlo Model.
**Journal of Optoelectronical Nanostructures. 2024; 9 (3): 77-95**
**DOI: 10.30495/JOPN.2024.33465.1318**

***Corresponding author:** Mohammad **Soroosh**
**Address:** Department of Electrical Engineering, Shahid Chamran University of Ahvaz, Ahvaz, Iran. **Tell:** 00989122965969 **Email:** m.soroosh@scu.ac.ir

## 1. INTRODUCTION

The Schottky junction as an electrical barrier in the path of the passage of electric carriers is considered a suitable option for reducing dark current or leakage current in devices. For example, in optical detectors where dark current determines the lower limit of the detector's power capability, the importance of this issue becomes more pronounced. Therefore, low dark current is one of the features of the Metal-Semiconductor-Metal (MSM) devices [1]. The small capacitance of the Schottky junction is an important parameter that leads to a better response of the device at high frequencies respect to high-speed optical devices [2-6]. Other features such as simple fabrication have led to the use of Schottky junction in semiconductor devices [7-9].

The use of a Schottky junction in MSM devices made of silicon and titanium dioxide-platinum has resulted in a reduction in dark current to around a few pico-amperes and an increase in signal-to-noise ratio [10,11]. This junction is also used as a barrier to reduce the gate current of field-effect transistors [12,13]. Reports have also indicated an increase in cutoff frequency and improved response of field-effect transistors [14-16]. The placement of a thin charge layer at the metal-semiconductor interface is an important issue that allows for the control of some of the characteristics of the Schottky junction. The effect of the charge layer with a different impurity concentration from the Schottky diode has caused a change in the thickness of the potential barrier of the Schottky junction and has shown that the potential barrier can be optimized. This change causes components such as tunneling current and consequently the current passing through the device to change [17,18].

Various reports have been presented on the simulation of devices with Schottky junctions, including a numerical drift-diffusion model for Schottky junctions. In this model, the spatial distribution of the average velocity and electron density is calculated by modifying the continuity equation. Although this model simulates a simple analysis of the behavior of a Schottky junction, it cannot microscopically examine the behavior of electrons [19,20]. The Monte Carlo method has been proposed as a microscopic method for simulating semiconductor devices with Schottky junctions. In a report, the radio frequency and noise performance of AlGaN/GaN Schottky junctions are simulated and analyzed using this method. The simulation shows that the use of a Schottky junction results in a lower noise device [21,22]. In another study, the full-band Monte Carlo (FBMC) method was used to calculate the current of a double-gate Schottky barrier tunneling transistor (DGSBTT). This report shows that the

tunneling mechanism plays a major role in the behavior of the device and that this structure has a better frequency response than the single-gate structure [23,24]. A two-valley Monte Carlo method has shown that using a Schottky junction in the source-drain channel of a MOSFET improves the device's frequency response and increases its bandwidth. This study also investigated the effect of channel length on the device's frequency response [25,26].

Carbon nanotube field effect transistors (CNTFETs) have gained remarkable attention in modern fields, as one of the promising candidates for replacing conventional MOSFET technology at the end of the roadmap. In this regard, Ghodrati and et. al present high-performance complementary logic gates based on ballistic gate-all-around CNTFETs utilizing a novel improved analytical model. This is done by considering the effects of carrier density, quantum capacitance, and the number of channels, which are highly suitable for logic applications [27]. Khaleqi Qaleh Jooq and et. al described in detail the different steps involved in the construction of a carbon nanotube field-effect transistor based on a network of single-walled CNTs (SWCNTs), which can selectively detect toxic gases. Due to the absorption feature of the allotropes of carbon, they can be used to make different devices. Absorbing materials by CNTs can change their electrical properties, which can be used in manufacturing chemical sensors. One specific type of electrochemical SWCNT sensor is the so-called CNTFET. The operation principle of these sensors is based on the changes in the I–V curves of nanotubes as a result of the adsorption of specific molecules on their surface [28].

Given the diverse applications of Schottky junctions in electronic devices, it seems necessary to provide a microscopic and accurate model or simulation for the behavior of electrical carriers in this junction. Although previous reports have used the Monte Carlo method to simulate devices with Schottky barriers, no detailed microscopic study of the behavior of carriers within this junction has been carried out to date. Therefore, simulating the behavior of carriers is an attractive and practical topic.

This work deals with the microscopic simulation of the current flowing through a Schottky junction with a GaAs semiconductor. Due to the low impurity concentration of GaAs, a potential barrier with a thickness of several hundred nanometers is formed. In this study, the tunneling and thermionic emission (TE) mechanisms are considered. The random nature of the various mechanisms within the semiconductor, such as tunneling, carrier scattering, and field-induced drift length, makes the choice of the Monte Carlo method for simulating electron behavior logical and acceptable. The Monte Carlo model can

show the movement of electrons in time and space on a frame-by-frame basis.

In the proposed model, the sequential drift and scattering mechanisms of electrons are investigated. In other words, after each drift, a scattering event occurs for the electron. The model presented takes into account scattering due to impurities, polar phonons, and acoustic phonons. Two valleys, Γ and L, are considered for electrons, and non-parabolic energy bands are taken into account. In the next section, the physics of the Schottky junction will be briefly introduced. The proposed model will then be described, and the results obtained will be explained in the final section.

## 2. THEORY OF SCHOTTKY JUNCTION

A Schottky junction is a metal-semiconductor junction in which the impurity concentration of the semiconductor is low. In this case, the work function of the metal is greater than the work function of the semiconductor, and an approximately triangular electrical barrier is formed at the junction. Figure 1 shows a diagram of the energy band diagram of a Schottky junction in equilibrium. When the metal-semiconductor junction is formed, some electrons are transferred from the semiconductor to the metal due to the equalization of the Fermi levels, and a depletion region is created at the boundary of the semiconductor with the metal. As a result, a bending of the conduction and valence bands of the semiconductor occurs.

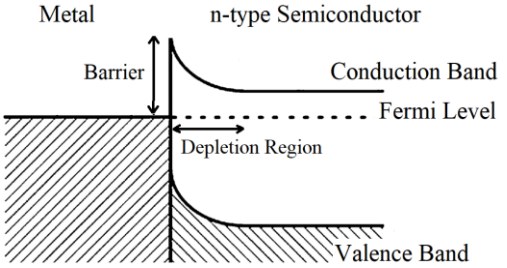


**Fig. 1**. Energy band diagram of a Schottky junction in equilibrium.

In a Schottky junction, there are thermionic emission, tunneling, and diffusion current components, of which thermionic emission and tunneling are the most important current mechanisms and dominate at high temperatures and thin barriers, respectively [29].

$$\varphi = \frac{KT}{q} Ln\left(\frac{A^* T^2}{J_S}\right) \quad (1)$$

where $A^*$ is the effective Richardson constant and its value is considered to be 8.2 $Acm^{-2}K^{-2}$. Parameters $T$, $K$, $q$, and $J_S$ are temperature in Kelvin, Boltzmann

constant, electron charge, and reverse saturation current density, respectively.

Even at room temperature, some electrons in the semiconductor have thermal energy exceeding the conduction band minimum. These hot electrons can overcome the work function of the semiconductor itself. If the thermal energy of an electron is sufficient to overcome both the semiconductor work function and the Schottky barrier height, it can be emitted into the metal.

## 3. The Monte Carlo Model

Monte Carlo is a numerical model that is used to analyze random phenomena and is based on a large number of repetitions. Given the randomness of various mechanisms such as drift, scattering, and tunneling of electrical carriers, the choice of this method for simulating a Schottky junction seems logical. In this work, 25000 super electrons (SE) are considered and they are moved simultaneously in sequential drift and scattering processes in the ensemble Monte Carlo (EMC) model. Each super electron represents a large number of electrons and the behavior of the super electron is attributed to them. The initial kinetic energy of the super electrons is considered to be the thermal energy from the environment. The spatial cell size and time step are chosen to be smaller than the Debye length and the inverse of the semiconductor plasma frequency, respectively. To calculate the spatial distribution of potential and electric field, Poisson's equation is discretized using the forward finite difference method, and the charge of each super electron is divided between its two adjacent nodes using the cloud-in-cell technique [30]. For simplicity of notation, the term "electron" will be used from now on instead of "super electron", but it is understood that the main concept refers to the super electron.

For the boundary points of the device, Neumann and Dirichlet conditions are applied [31]. In other words, the normal component of the electric field is considered to be zero at the boundary points that do not have a metal connection, and the tangential component of the electric field is considered to be zero at the metal connection points. Also, the collision of the super particle with the semiconductor walls is reflected like the reflection of light from a mirror. Using the Wentzel-Kramers-Brillouin probability function for the tunneling of electrons, a triangular approximation for the Schottky barrier is used [29]. The probability function is calculated based on the energy of the electrons and their distance from the metal, and the rejection/acceptance technique is used to decide whether the electron reaches the metal. This probability is calculated for electrons that are in the depletion region and have energy less than the potential barrier. Electrons that cannot pass through the barrier are reflected back due to

the collision with the barrier by mirroring their wave vector in the direction of the collision.

The accumulation of positive charges in the atomic nuclei, the presence of impurity atoms, and the vibration of crystal atoms in the crystal structure cause an effective Coulomb force to act on the electrons and deflect them from their path. According to quantum mechanics, these forces can be considered as perturbation potentials. As a result, these forces are considered in the form of electron scattering mechanisms, and the scattering rates due to impurities, acoustic phonons, non-polar optical phonons, and polar optical phonons are selected to form the scattering matrix. The rates of these scatterings are fully described in reference [32]. Each relevant scattering mechanism has a corresponding scattering rate. This rate depends on the particle's energy and is calculated beforehand. These rates are often stored in a table for efficient access during the simulation. After a particle completes a free flight, a random number between 0 and 1 is generated. The inverse cumulative distribution function of the total scattering rate is not directly used, but the concept is involved. The random number is compared to the accumulated scattering rates for each mechanism, starting from the highest rate. If the random number falls within the accumulated rate of a specific mechanism, that mechanism is chosen for the scattering event. This ensures that mechanisms with higher rates have a higher probability of being selected.

The presence of significant electric fields in the depletion region of the Schottky junction allows electrons to gain kinetic energy greater than 0.3 eV, so electrons can be transferred from the central valley Γ to the valley L. As a result, a two-valley model is used for simulation. The energy bands are considered non-parabolic to achieve higher accuracy in the relationship between momentum and kinetic energy of electrons.

The number of electrons adjacent to the junction is checked after each drift and scattering process, and their number is kept constant. This condition is to keep the potential of the junction constant during the simulation. To calculate the electric current for an applied potential to the device, the product of the total number of electrons leaving it and their charge is divided by the duration of the simulation.

Table I shows the overall simulation steps. First, the dimensions of the junction, its parameters such as the material-dependent physical constants, and the initial kinetic energy of the electrons are determined. Then, the scattering matrix is formed based on the energy steps. Next, the iterative drift and scattering process is performed at each time step. At the end of each time step,

the Neumann and Dirichlet boundary conditions are applied, and the distribution of electrons is obtained. The distribution of electric charge is calculated by assigning the electron charge to their neighboring nodes, and the distribution of potential and electric field is simulated by discretizing Poisson's equation. The electric field obtained at the end of each time step is used as the driving force for the electrons in the next time step. This process continues until the end of the simulation time.

**TABLE I**
**All steps for simulation of the Schottky junction using EMC.**

| Step | Work |
|---|---|
| 1 | Discretization of the device, Determination of the concentration density |
| 2 | Determination of SEs per cell, Assigning a random energy, a wavevector, and a space to each SE |
| 3 | Definition of Scattering Matrix |
| 4 | Drift-Scattering process for SEs within a time step |
| 5 | Removing the outcoming SEs, Assigning energy, wavevector, and space to the new SEs |
| 6 | Applying Neumann and Dirichlet boundary conditions |
| 7 | Assigning the electric charge of SEs to the related nodes |
| 8 | Solving Poisson's equation, and calculation of electric and potential values in each cell |
| 9 | Repeating steps 4 to 7 for a certified time |

## 4. RESULTS AND DISCUSSIONS

A Schottky diode as shown in Figure 2 is considered for the simulation, and its parameters are presented in Table II. The right and left junctions are Schottky and ohmic, respectively. A potential difference $V_b$ is applied between the two contacts to create an electric field in the structure, which drives the electrons and forms an electric current.

Schottky diodes excel in low-voltage power supplies due to their inherently lower forward voltage drop compared to p-n junction diodes. This translates to higher efficiency and less wasted power as heat. They're commonly found in switching power supplies for computers, laptops, and LCD displays. Similar to power supplies, the low forward voltage drop makes them suitable for battery chargers, particularly for Lithium-ion batteries with lower operating voltages. Moreover, the fast-switching speed and minimal charge carrier storage in Schottky diodes make them ideal for high-frequency circuits like mixers and detectors used in radio frequency communication systems. By examining the various applications of the Schottky diode and its required sizes in each section, the sizes of the typical simulated Schottky device have been selected. The

temperature equals 300 K which is a common value in many articles. The spatial cell size is chosen to be smaller than the Debye length ($L_D$=96.03 nm). The time step has to be smaller than the inverse of the semiconductor plasma frequency ($1/\omega_p$=10.28 fs).

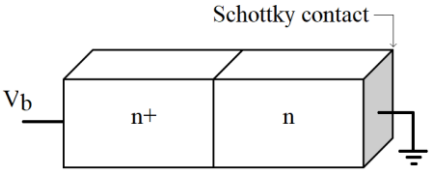


**Fig. 2**. A two-dimensional view of a Schottky diode with bias $V_b$.

**TABLE II**
**The used parameters for the simulation of the Schottky diode.**

| Parameter | Value | Parameter | | Value |
|---|---|---|---|---|
| Temperature | 300 °K | Length | n-region | 900 nm |
| Mesh cell | 5 nm | Concentration | n-region | $2\times10^{16}$ $cm^{-3}$ |
| Time step | 2 fs | Length | $n^+$-region | 300 nm |
| Number of iterations | 5000 | Concentration | $n^+$-region | $10^{18}$ $cm^{-3}$ |
| Number of SEs | 25000 | | | |

Figure 3 shows the spatial distribution of electron density for the equilibrium case and the application of a 5 V reverse bias. Due to the difference in Fermi levels between the metal and semiconductor in the Schottky junction and the migration of electrons from the semiconductor to the metal, a depletion region is created at the right end of the device, with a length of 0.22 µm and 0.58 µm in equilibrium and under bias, respectively. The low electron concentration in this region confirms the claim that it is depleted. These dimensions are in agreement with reference [29].

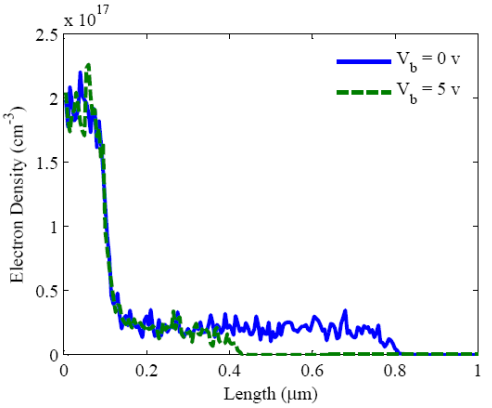


**Fig. 3**. Spatial distribution of carrier concentration in equilibrium and 5 V reverse bias.

Figures 4a and 4b show the spatial distribution of the potential and electric field of the device for different reverse voltages. The presence of the depletion region causes a potential drop and an increase in the electric field at the right end of the device. As the reverse voltage increases, the depletion region becomes larger and the intensity of the electric field increases. Figure 4b shows that there is another depletion region at the boundary of the n and n+ regions (i.e., over a length of 0.1 μm), which causes a small peak in the electric field distribution.

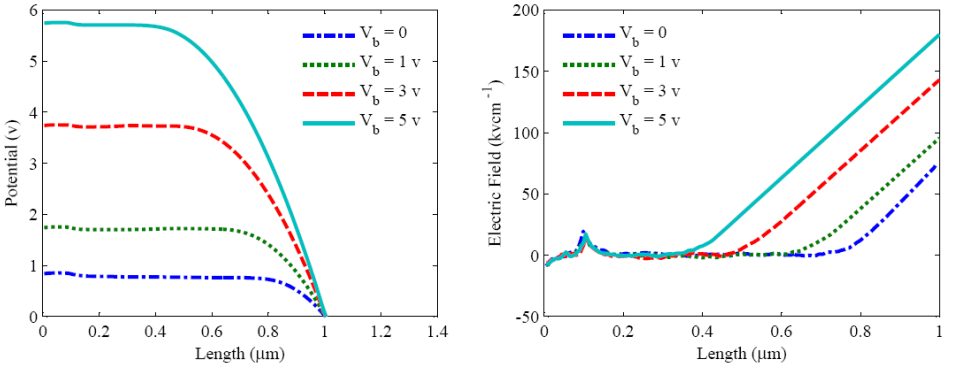


(a) (b)

**Fig. 4**. Distribution of (a) electric potential and (b) electric field intensity for reverse voltages of 0, 1, 3, and 5 V.

Table III compares the calculated barrier height and maximum electric field intensity for the device in Figure 4 for different reverse biases with an analytical model [29]. It is observed that the values obtained from the simulation are consistent with the analytical results.

**TABLE III**

**Comparison of barrier height and maximum electric field intensity obtained from the model with the results of reference [29].**

| Bias voltage (V) | Barrier (V) | | Maximum electric field ($kVcm^{-1}$) | |
|---|---|---|---|---|
| | EMC | Ref [17] | EMC | Ref [17] |
| 0 | 0.717 | 0.716 | 66.908 | 66.912 |
| 1 | 1.718 | 1.718 | 92.831 | 92.834 |
| 3 | 3.714 | 3.715 | 139.726 | 139.732 |
| 5 | 5.718 | 5.716 | 175.806 | 175.809 |

Figure 5 compares the calculated current density with the Monte Carlo model for two devices A and B with impurity concentrations of $2\times10^{16}$ $cm^{-3}$ and $5\times10^{16}$

$cm^{-3}$ for the n-region with the result obtained from the Silvaco software. Table 4 compares the calculated reverse saturation current density, junction built-in voltage, and effective Schottky barrier height for the two devices A and B with different impurity concentrations for the n-region with the results obtained from the Silvaco software. From Figure 5 and Table IV, it is concluded that with increasing impurity concentration of the n-region, tunneling increases due to the decrease of the depletion region, which causes a decrease in the effective barrier height or an increase in the current of device B compared to A at reverse bias and reverse saturation current.

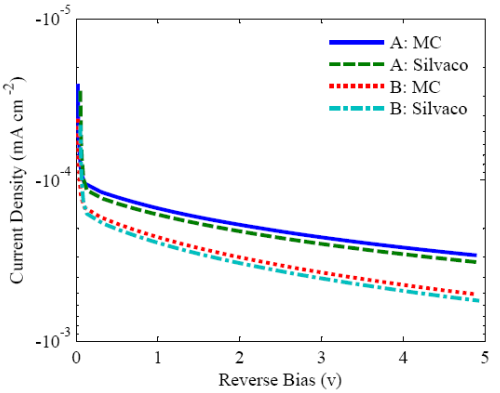


**Fig. 5**. Comparison of current density obtained from the Monte Carlo model with Silvaco software for devices A and B.

**TABLE IV**
**Calculation and comparison of parameters of devices A and B.**

| Device | Concentration of n-region ($cm^{-3}$) | Model or Software | Saturated reverse current density ($mAm^{-2}$) | Built-in-potential (V) | Schottky Barrier (eV) |
|---|---|---|---|---|---|
| A | $2\times10^{16}$ | EMC | $2.851\times10^{-5}$ | 0.725 | 0.806 |
| | | Silvaco | $2.874\times10^{-5}$ | 0.727 | 0.803 |
| B | $5\times10^{16}$ | EMC | $7.032\times10^{-5}$ | 0.717 | 0.775 |
| | | Silvaco | $7.103\times10^{-5}$ | 0.716 | 0.771 |

Table V shows the percentage contribution of thermionic emission and tunneling current components at different voltages for device A. The simulation shows that the contribution of the thermionic emission component is greater than that of tunneling. As the reverse voltage increases, the electric field intensity increases, and the probability of electron tunneling through the Schottky barrier increases. Therefore, as shown in Table V, the contribution of

the tunneling component increases with increasing voltage, and the contribution of the thermionic emission component decreases.

**TABLE V**
**Percentage contribution of thermionic emission and tunneling components in device A for different reverse voltages.**

| Reverse bias (V) | Thermionic (%) | Tunneling (%) |
|---|---|---|
| 1 | 67.37 | 32.63 |
| 3 | 58.6 | 41.4 |
| 5 | 53.36 | 46.64 |

Table VI shows the percentage distribution of electrons for the central and L valleys at equilibrium and a reverse voltage of 5 V. At equilibrium, 41.99% of the electrons are in the central valley and 0.59% of the electrons are in the L valley. Under a reverse bias of 5 V, 94.73% of the electrons are in the central valley and 5.26% of the electrons are in the L valley. As can be seen, at equilibrium, impurity scattering is the dominant mechanism, but with increasing bias voltage, the percentage of this scattering decreases. In fact, with an increasing electric field, the drift velocity of electrons increases, and the effect of the impurity atom Coulomb potential on the passing electrons has a shorter time effect, resulting in a decrease in the percentage of impurity scattering.

**TABLE VI**
**Percentage scattering of electrons by different mechanisms at equilibrium and for a reverse voltage of 5 V.**

| Scattering mechanism | | Impurity | | Acoustic | | Optical phonon | | | | | | | | | |
|---|---|---|---|---|---|---|---|---|---|---|---|---|---|---|---|
| | | | | | | Polar | | | | | | Non-polar | | | |
| | | | | | | Intra-valley | | | | Inter-valley | | Intra-valley | | Inter-valley | |
| | | | | | | Emission | | Absorption | | Emission | Absorption | Emission | Absorption | Emission | Absorption |
| Valley | | Γ | L | Γ | L | Γ | L | Γ | L | Γ | Γ | L | L | L | L |
| % | $V_b$=0 V | 72 | 59 | <1 | 3 | 15 | 9 | 10 | 8 | <1 | <1 | 9 | 9 | 2 | 1 |
| | $V_b$=5 V | 58 | 33 | 1 | 5 | 14 | 14 | 8 | 6 | 12 | 6 | 24 | 12 | 4 | 2 |

With the applied bias to the device, the electric field intensity increases, and with the increase in the kinetic energy of the electrons, the probability of their transfer from the central valley to the L valley also increases. As a result, the percentage of scattering caused by inter-valley optical phonons increases until, for large electric fields, the contribution of inter-valley optical phonon emission becomes significant and causes the transfer of a portion of the electrons from the central valley to the L valley with lower mobility. This causes the average electron velocity to reach saturation. In general, it can be said that with increasing electric field intensity, the contribution of impurity scattering decreases, and the contribution of other scattering mechanisms such as acoustic and non-polar optical scattering increases.

Figure 6 shows the spatial distribution of electron energy at equilibrium and for a reverse voltage of 5 V. At equilibrium, with the weak electric field dominating the depletion region, the maximum electron energy is about 0.63 eV. With the applied reverse bias to the device and the dominance of the strong electric field in the depletion region, the electron energy increases. The farther away from the depletion region, the electric field intensity (Figure 6b) and electron energy also decrease.

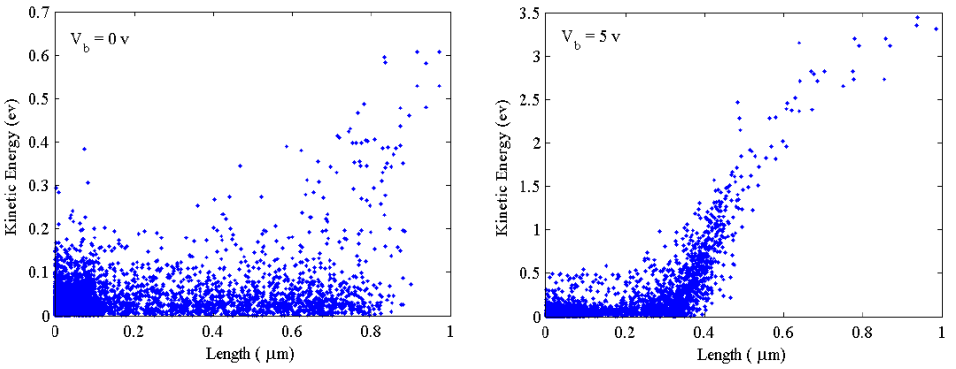


(a) (b)

**Fig. 6**. Spatial distribution of electron kinetic energy for (a) equilibrium and (b) reverse voltage of 5 V.

Figure 7 shows the velocity as a function of electron kinetic energy for equilibrium and reverse voltage of 5 V. It can be seen that at equilibrium, due to the low electron energy, most of them are in the central valley and in the energy range of less than 0.1 eV. However, with the applied reverse bias and the increase in electric field intensity, electrons can be transferred to a space farther

away from the minimum energy range and placed in the L valley. Figures 7 and 8 show that with increasing device voltage and electric field intensity, electron kinetic energy increases, and electrons can be transferred to the L valley (by inter-valley mechanisms). Therefore, with increasing electric field intensity, the percentage of electron presence in the central valley decreases and increases in the L valley.

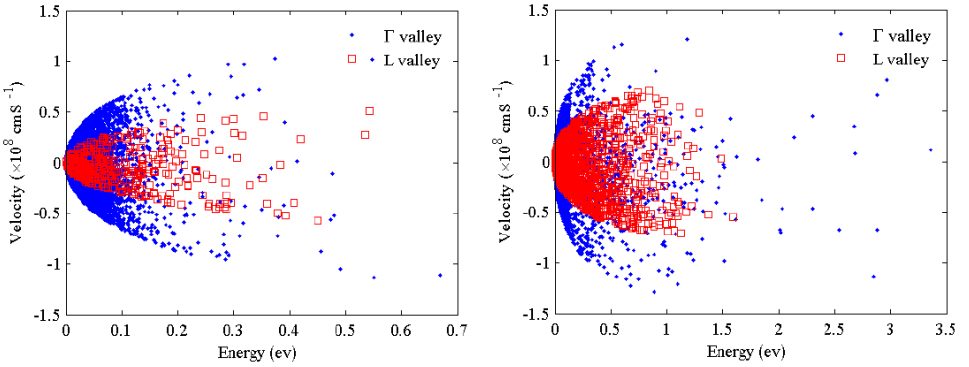


**Fig. 7**. Distribution of velocity as a function of electron energy for (a) equilibrium and (b) reverse voltage of 5 V.

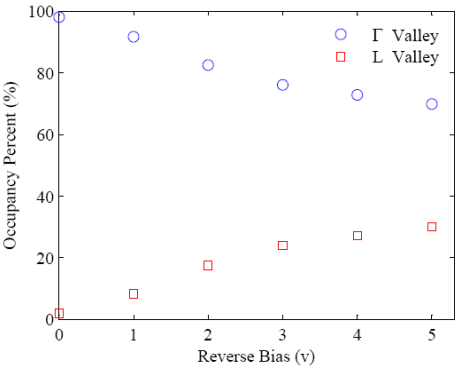


**Fig. 8**. Percentage presence of electrons in central and satellite valleys for different reverse voltages.

To show the stability of the proposed structure, the temperature parameter is one of the most significant external parameters that is considered and investigated. The simulation results are reported in Table VII for GaAs Schottky junction with the carrier concentration of $2\times10^{16}$ $cm^{-3}$.

**TABLE VII**
**The effect of temperature on the saturated reverse current density, built-in potential, and Schottky barrier.**

| Temperature (k) | Saturated reverse current density ($mAcm^{-2}$) | Built-in-potential (V) | Schottky barrier (eV) |
|---|---|---|---|
| 200 | $3.768\times10^{-13}$ | 0.765 | 0.850 |
| 250 | $1.340\times10^{-8}$ | 0.752 | 0.836 |
| 300 | $2.851\times10^{-5}$ | 0.725 | 0.806 |

At higher temperatures, more electrons in the metal gain enough thermal energy to overcome the potential barrier and enter the semiconductor. This reduces the effectiveness of the barrier in blocking current flow. With rising temperature, the vibrations of atoms in the semiconductor lattice increase. This can slightly alter the spatial distribution of charges in the depletion region, effectively reducing its width. A narrower depletion region translates to a lower potential barrier for electrons to overcome. Generally, increasing temperature increases the current density. This follows from the lowering of the Schottky barrier height with rising temperature. With a smaller barrier, more electrons in the metal can overcome it and contribute to the current flow across the junction. This translates to a higher current density. We can explain this with the concept of thermionic emission, the dominant current conduction mechanism in Schottky junctions. Thermionic emission describes the process where electrons with sufficient thermal energy escape the metal and enter the semiconductor. A lower barrier height due to higher temperature allows more electrons to satisfy this energy requirement, leading to a rise in current density.

Based on the simulation results, it can be concluded that the proposed model can accurately simulate the movement of electrons and the passage through the Schottky barrier with a microscopic view. The ability to display the spatial distribution of electron density and energy, the distribution of energy by electron velocity, the spatial distribution of potential and electric field intensity, and the current-voltage curve of the Schottky diode are among the most important features of the Monte Carlo model. Calculation of the contribution of scattering mechanisms for different conditions and tracking the random motion path of electrons are special capabilities of the Monte Carlo model. The statistical view of the device by the model makes it possible to interpret the physical behavior of electrons, and the designer can see the effect of any change in the device on the behavior of electrons and not just focus on the average value of the parameters.

Based on the regular and known process of simulation steps (as shown in table I), the behavior of other devices can also be simulated microscopically by developing the proposed model. Providing a statistical distribution for the behavior of electrons makes it possible to accelerate the development of the model by interpreting the statistical results. Therefore, the authors believe that the proposed model is an effective tool for analyzing the behavior of electrons in passing through the Schottky barrier, which, in addition to accuracy, can be developed and generalized to other semiconductor devices.

## 5. CONCLUSION

In this study, an ensemble Monte Carlo model is presented by considering two central and L valleys for electrons and scattering caused by impurities and phonons. By simulating the drift and scattering mechanisms, it can solve the Boltzmann transport equation in the Schottky diode and accurately show how electrons pass through the Schottky barrier. The proposed model can provide the distribution of various parameters of each electron, such as the spatial distribution of density, potential, and electric field. Based on the results obtained from the model, it is observed that increasing the electric field intensity increases the probability of electron presence in the L valley due to the increase in the contribution of inter-valley scattering. Also, the non-parabolicity of the energy-velocity relationship increases with increasing electron energy. The proposed model shows that increasing the reverse voltage increases the depletion region of the Schottky diode and increases the probability of tunneling of electrons that are accelerated in this region, as a result of which the contribution of the tunneling current component increases.

## ACKNOWLEDGMENT

This work was supported by Shahid Chamran University of Ahvaz, grant number SCU.EE1402.672.

## REFERENCES

[1] A. S. Razeen, E. X. Tang, G. Yuan, J. Ong, K. Radhakrishnan, and S. Tripathy. *Self-powered action in metal-semiconductor-metal ultraviolet photodetectors based on AlGaN/GaN high electron mobility transistor structures on different substrates*. Optical Materials, 150 (2024) 115135. Available: https://doi.org/10.1016/j.optmat.2024.115135

[2] M. J. Maleki, M. Soroosh, G. Akbarizadeh, F. Parandin, and F. Haddadan. *Photonic Crystal Resonators in Designing Optical Decoders*. Journal of Optoelectronical Nanostructures, 8(4) (2023) 1-24. Available: https://doi.org/10.30495/JOPN.2023.32220.1296

[3] F. Pakrai, M. Soroosh, and J. Ganji. *Designing of all-optical subtractor via PC-based resonators*. Journal of Optoelectronical Nanostructures, 7(2) (2022) 21-36. Available: https://doi.org/ 10.30495/JOPN.2022.29545.1246

[4] M. Soroosh, A. Mirali, and E. Farshidi. *Ultra-Fast All-Optical Half Subtractor Based on Photonic Crystal Ring Resonators*. Journal of Optoelectronical Nanostructures, 5(1) (2020) 83-100. Available: https://jopn.marvdasht.iau.ir/article_4035.html

[5] S. M. H. Jalali, M. Soroosh, and Gholamreza Akbarizadeh. *Ultra-fast 1-bit comparator using nonlinear photonic crystal based ring resonators*. Journal of Optoelectronical Nanostructures, 4(3) (2019) 59-72. Available: https://jopn.marvdasht.iau.ir/article_3620.html

[6] E. Rafiee and F. Abolghasemi. *An All-Optical NOR Gate based on Two-Dimensional Photonic Crystals*. Journal of Optoelectronical Nanostructures, 8(1) (2023) 47-57. Available: https://doi.org/10.30495/JOPN.2023.31310.1275

[7] A. Kosarian. Complete Guide to Semiconductor Devices. 1st ed. Shahid Chamran University of Ahvaz press. 51-69, 2008 (in Persian). Available: https://onlinelibrary.wiley.com/doi/book/10.1002/9781118014769

[8] F. Haddadan, M. Soroosh, and N. Alaei-Sheini, *Designing an electro-optical encoder based on photonic crystals using the graphene-$Al_2O_3$ stacks*. Appl. Opt. 59(7) (2020) 2179-2185. Available: https://doi.org/10.1364/AO.386248

[9] M. Soroosh, A. Farmani, M.J. Maleki, F. Haddadan, and M. Mansouri, Highly Efficient Graphene-Based Optical Components for Networking Applications. In Photonic Crystal and Its Applications for Next Generation

Systems, Singapore: Springer Nature Singapore, 15-35, 2023. Available: https://doi.org/10.1007/978-981-99-2548-3_2

[10] S. Pal, S. Jana, R. Kamparath, S. Bhunia, N. Sharma, S. Karwal, A. Shaikh, and N. Benerji. *PMMA as an Additive for Nanostructured $TiO_2$ Thin Films for Heterojunction Visible-Blind Photodetectors*. ACS Applied Nano Materials. 7(3) (2024) 3339–3351. Available: https://doi.org/10.1021/acsanm.3c05745

[11] F. Haddadan and M. Soroosh, *Design and simulation of a subwavelength 4-to-2 graphene-based plasmonic priority encoder*. Opt. Laser Technol. 157 (2023) 108680. Available: https://doi.org/10.1016/j.optlastec.2022.108680

[12] M. Li, W. Luo, X. Zhang, M. Zhu, G. Peng, Z. Zhu, and S. Qin. *Control of Carrier Polarity and Schottky Barriers in Layered $PdSe_2$ Field-Effect Transistors*. Applied Electronic Materials. 5(6) (2023) 3394-3402. Available: https://doi.org/10.1021/acsaelm.3c00401

[13] F. Haddadan, M. Soroosh, and N. Alaei-Sheini, *Cross-talk reduction in a graphene-based ultra-compact plasmonic encoder using an Au nano-ridge on a silicon substrate*. Appl. Opt. 61(11) (2022) 3209-3217. Available: https://doi.org/10.1364/AO.449123

[14] J. Zhu, J. Ning, D. Wang, J. Zhang, L. Guo, Y. Hao. *High-performance two-dimensional InSe field-effect transistors with novel sandwiched ohmic contact for sub-10 nm nodes*: *a theoretical study*. Nanoscale Research Letters. 14 (2019) 1-8. Available: https://doi.org/10.1186/s11671-019-3106-8

[15] F. Bagheri, M. Soroosh, F. Haddadan, and Y. Seifi-Kavian, *Design and simulation of a compact graphene-based plasmonic D flip-flop*. Opt. Laser Technol. 155 (2022) 108436. Available: https://doi.org/10.1016/j.optlastec.2022.108436

[16] A. Mondal, C. Biswas, S. Park, W. Cha, S. H. Kang, M. Yoon, S. H. Choi, K. K. Kim, and Y. H. Lee. *Low Ohmic contact resistance and high on/off ratio in transition metal dichalcogenides field-effect transistors via residue-free transfer*. Nature Nanotechnology. 19(1) (2024) 34-43. Available: https://doi.org/10.1038/s41565-023-01497-x

[17] M. J. Maleki, M. Soroosh, G. Akbarizadeh, F. Parandin, and F. Haddadan, Photonic crystal-based decoders: ideas and structures. Recent Advances and

Trends in Photonic Crystal Technology: Intech Open 1-18 (2023). Available: https://doi.org/10.5772/intechopen.1002401

[18] B. Han, Y. Zhao, C. Ma, C. Wang, X. Tian, Y. Wang, W. Hu, and P. Samorì. *Asymmetric Chemical Functionalization of Top‐Contact Electrodes: Tuning the Charge Injection for High‐Performance $MoS_2$ Field‐Effect Transistors and Schottky Diodes*. Advanced Materials. 34(12) (2022) 2109445. Available: https://doi.org/10.1002/adma.202109445

[19] F. Hadadan, and M. Soroosh, *A new proposal for 4-to-2 optical encoder using nonlinear photonic crystal ring resonators*. IJOP 13(2) (2019) 119-126. https://doi.org/10.29252/ijop.13.2.119

[20] A. Mahmoodpoor and S. Makarov. *Numerical analysis of charge carriers injection in a light emitter or detector device based on a metal-semiconductor-metal structure*. Photonics and Nanostructures-Fundamentals and Applications, 58 (2024) 101213. Available: https://doi.org/10.1016/j.photonics.2023.101213

[21] F. Haddadan, M. Soroosh, and M.J. Maleki, Presenting a two-valley Monte Carlo model for simulating and analyzing electron behavior in GaAs bulk and investigating the effects of electron transitions (Gunn Effect). 1st international and 7th national conference Congress on Electrical Engineering and Intelligent Systems. Iran. Najafabad (2024). Available: https://civilica.com/doc/1963406

[22] D. Shaikshavali and D. Kannadassan. *Influence of surface trap states on RF/microwave performance of lateral AlGaN/GaN Schottky barrier diode*. Journal of Electromagnetic Waves and Applications. 36(1) (2022) 29-47. Available: https://doi.org/10.1080/09205071.2021.1956374

[23] F. Haddadan, F. Bagheri, A. Basem, H.A. Kenjrawy, and M. Soroosh, *Evanescent field engineering to reduce cross-talk in pattern-free suspended graphene-based plasmonic waveguides using nano-strips*. International Journal for Light and Electron Optics 313 (2024) 171989. Available: https://doi.org/10.1016/j.ijleo.2024.171989

[24] G. Du, X. Liu, M. Liu, L. Sun, and R. Han. *Characterizations of Double-gate SBTT Studying by a 2-D Full-Band Monte Carlo Device Simulator*. The Fourth International Workshop on Junction Technology, Shanghai, China. (2004) 325-327. Available: https://ieeexplore.ieee.org/document/1306871

[25] H. Takeda, T. Ikezawa, M. Kawada, and M. Hane. *Source/Drain Engineering for High-Performance Deep sub-100nm Ge-pMOSFETs Using Full-Band Monte Carlo Simulation.* IEEE International Conference on Semiconductor Engineering. Kanagawa, Japan. (2008) 113-116. Available: https://ieeexplore.ieee.org/document/4648250

[26] F. Haddadan, and M. Soroosh, *Low-power all-optical 8-to-3 encoder using photonic crystal-based waveguides*. Photonic Network Communications 37 (2019) 83-89. Available: https://doi.org/10.1007/s11107-018-0795-3

[27] M. Ghodrati, A. Mir, and A. Farmani. Carbon nanotube field effect transistors–based gas sensors. In nanosensors for Smart Cities (2020) 171-183). Available: https://doi.org/10.1016/B978-0-12-819870-4.00036-0

[28] M. Khaleqi Qaleh Jooq, A. Mir, S. Mirzakuchaki, and A. Farmani. Semi-analytical modeling of high performance nano-scale complementary logic gates utilizing ballistic carbon nanotube transistors. Physica E: Low-dimensional Systems and Nanostructures (2018) 104, 286-296. Available: https://doi.org/10.1016/j.physe.2018.08.008

[29] S. M. Sze and K. K. Ng. Physics of Semiconductor Devices. 4th ed. John Wiley & Sons, (2019) 134-181. Available: https://www.amazon.com/Physics-Semiconductor-Devices-Simon-Sze/dp/0471143235

[30] K. Tomizawa. Numerical Simulation of Submicron Semiconductor Device. 1st ed. Artech House, (1993) 38-69. Available: https://www.amazon.com/Numerical-Simulation-Submicron-Semiconductor-Materials/dp/0890066205

[31] C. Moglestue. Monte Carlo Simulation of Semiconductor Device. 1st ed. Chapman & Hall, (1993) 115-129. Available: https://link.springer.com/book/10.1007/978-94-015-8133-2

[32] D. Vasileska, S. M. Goodnick, and G. Klimeck. Computational Electronics Semi Classical and Quantum Device Modeling and Simulation. CRC Press, (2010) 241-332. Available: httpss://doi.org/10.1201/b13776